VACUUM ENERGY IN GENERAL POWER WALL MODELS

An Undergraduate Research Scholars Thesis

by

AGAM SHAYIT

Submitted to the LAUNCH: Undergraduate Research office at
Texas A&M University
in partial fulfillment of the requirements for the designation as an

UNDERGRADUATE RESEARCH SCHOLAR

Approved by
Faculty Research Advisors: Stephen Fulling
Vivek Sarin

May 2021

Majors: Computer Science
Physics

RESEARCH COMPLIANCE CERTIFICATION

Research activities involving the use of human subjects, vertebrate animals, and/or biohazards must be reviewed and approved by the appropriate Texas A&M University regulatory research committee (i.e., IRB, IACUC, IBC) before the activity can commence. This requirement applies to activities conducted at Texas A&M and to activities conducted at non-Texas A&M facilities or institutions. In both cases, students are responsible for working with the relevant Texas A&M research compliance program to ensure and document that all Texas A&M compliance obligations are met before the study begins.

I, Agam Shayit, certify that all research compliance requirements related to this Undergraduate Research Scholars thesis have been addressed with my Research Faculty Advisors prior to the collection of any data used in this final thesis submission.

This project did not require approval from the Texas A&M University Research Compliance & Biosafety office.

TABLE OF CONTENTS

ABSTRACT

Vacuum Energy in General Power Wall Models

Agam Shayit
Department of Computer Science and Engineering
Department of Physics and Astronomy
Texas A&M University

Research Faculty Advisor: Dr. Stephen Fulling
Department of Mathematics
Texas A&M University

Research Faculty Advisor: Dr. Vivek Sarin
Department of Computer Science and Engineering
Texas A&M University

In the study of vacuum energy and the Casimir effect, it proves convenient to model the parallel conducting plates by a "soft" wall of the form $v(z) = z^\alpha$ rather than the standard Dirichlet wall. This model, for instance, does not violate the principle of virtual work under regularization, unlike the naive Dirichlet model.

In previous research, the soft wall model was formalized for a massless scalar field, and expressions for the corresponding stress tensor were derived. Using these expressions, the energy density and pressure were calculated inside and out of the wall for the linear and quadratic walls, for which exact solutions exist.

The limit of interest is $\alpha \gg 1$, which corresponds to the Dirichlet wall. Since a closed form expression for the Green function of the field equation cannot be found for $\alpha > 2$, one must approximate it in order to use the previously derived expressions for the stress tensor.

In this thesis, we conclude this research project. Using high order WKB and perturbation

expansions of the associated Green function, we develop a robust approximation scheme in the regime where neither is valid. This approximation matches both expansions to an appropriate order in their domain of validity.

We apply the developed scheme to the sextic soft wall and use it to compute the stress tensor inside the cavity for various conformal parameters. The consistency of the results is verified by checking known conservation laws and reproducing the energy density for the quadratic wall.

To further verify our results, we compare the approximated stress tensor to a numerical counterpart, which is obtained by discretizing the separated field equation. To maximize accuracy and efficiency, we develop a customized numerical stiff linear boundary value solver which exploits key properties of the field equation. This solver is implemented in two different ways, which prioritize the concurrency of the solution process and the accuracy of the output.

ACKNOWLEDGMENTS

Contributors

I would like to thank my faculty advisors, Dr. Fulling and Dr. Sarin, for their guidance, support, and availability. I would also like to thank K. A. Milton for providing constructive feedback, as well as the data from an earlier paper, which is used in Fig. 4.7 for comparison purposes. Thanks also go to Tommy Settlemyre, who provided me guidance in the early stages of this research, and whose previous unpublished work on the application of Padé approximants to the soft wall model played an important role in this thesis.

Funding Sources

This research was supported in part by the summer 2020 stipend from the Physics and Astronomy department at Texas A&M University. The numerical portion of this work relied on the advanced computing resources provided by Texas A&M High Performance Research Computing. This work is otherwise unfunded.

1. INTRODUCTION

1.1 The Casimir Effect

The Casimir effect in Quantum Field Theory refers to the attractive force between the boundaries of a cavity in vacuum. This attractive force is induced by the energy gradient resulting from the modification of the normal modes of the quantum field inside the cavity. The existence of this force entails that the expectation value of the quantum field is nonzero in vacuum. This force was first derived by Casimir in [1] for an electromagnetic field and perfect conductor. Many later works, such as [2], [3], and [4], simplify Casimir's model by replacing the EM field and the conductor with a scalar field and Dirichlet boundary conditions.

In order to produce physical results in models in quantum field theory, one must regularize them first. This is most commonly done by imposing an ultraviolet cutoff, which prevents subtraction of infinite quantities. Since the scalar field with Dirichlet boundary conditions ("hard wall") model was shown in [5] to violate the principle of virtual work under ultraviolet cutoffs, it is unsuitable for contemporary analysis of phenomena in Casimir physics. Since the Casimir force is dominant in small scales, its analysis under a physically consistent model may aid in the discovery of new fundamental forces of nature. In this paper, we restrict our analysis to a single massless scalar field. This quantum field is denoted by ϕ.

1.2 The Soft Wall Model

To overcome the violation of the principle of virtual work under regularization, it was proposed in [6] and [7] to replace the ideal Dirichlet wall with the "softer" counterpart

$$v(z) = z^{\alpha} \qquad \alpha \in \mathbb{N} \tag{1.1}$$

Unlike the Dirichlet wall, the soft wall was shown to uphold the principle of virtual work under ultraviolet cutoffs (see [8]). This makes the model consistent with contemporary physics and suitable for a modern analysis of the Casimir effect.

In previous research ([8], [9], [10]), the soft wall model was developed for a massless scalar field. The reduced Green function of the field equation inside the wall was derived in [7] as

$$g_\kappa(z) = \frac{1}{w}\left(F(z)G(z) - F(z)^2\frac{G(0) - G'(0)/\kappa}{F(0) - F'(0)/\kappa}\right) \tag{1.2}$$

Here, $\kappa > 0$ is the analytically continued frequency parameter, z is the displacement along the axis perpendicular the wall, and w is the Wronskian of $F(z), G(z)$, which are solutions of the differential equation

$$-\frac{\partial^2 y}{\partial z^2} + \left(\kappa^2 + v(z)\right) y = 0 \tag{1.3}$$

such that F decays at positive infinity and G is linearly independent of F. Although the solutions $F(z), G(z)$ also depend on κ, this dependence is usually suppressed in the notation.

By normalizing the boundary conditions of $F(z), G(z)$ to be

$$G(0) = 0 \qquad G'(0) = 1 \qquad F(0) = 1 \tag{1.4}$$

(1.2) was simplified to

$$\begin{aligned} g_\kappa(z) &= F(z)G(z) + \gamma(\kappa)F(z)^2 \\ \gamma(\kappa) &= \frac{1}{\kappa - F'(0)} \end{aligned} \tag{1.5}$$

As shown in [9], the vacuum expectation value $\langle\phi^2\rangle$ is given by $I\left[g_\kappa(z)\right]$ and the scalar δ, where

$$I\left[h(\kappa)\right] \equiv \frac{1}{2\pi^2}\int_0^\infty d\kappa\ \kappa^2 h(\kappa)\frac{\sin\kappa\delta}{\kappa\delta} \tag{1.6}$$

Expressions for the components of the corresponding renormalized stress tensor within the wall were also derived (see (5.11) in [9]). These expressions involve terms of the form

$$I\left[\kappa^a f(z)\frac{\partial^b\left(g_\kappa(z) - \tilde{g}_\kappa(z)\right)}{\partial z^b}\right] = \frac{1}{2\pi^2}\int_0^\infty d\kappa\ \kappa^{a+2} f(z)\frac{\partial^b\left(g_\kappa(z) - \tilde{g}_\kappa(z)\right)}{\partial z^b}\frac{\sin\kappa\delta}{\kappa\delta} \tag{1.7}$$

where $a, b \in \{0, 2\}$, the function $f(z)$ is either a constant or the soft wall potential (1.1), and $\tilde{g}_\kappa(z)$ is the asymptotic behavior of the Green function. The last is given in (3.1) in [9] as

$$\tilde{g}_\kappa(z) = \frac{\alpha^2 z^\alpha \left(z^\alpha - 4\kappa^2\right) + 4\alpha z^\alpha \left(z^\alpha + \kappa^2\right) + 32 z^2 \left(z^\alpha + \kappa^2\right)^3}{64 z^2 \left(z^\alpha + \kappa^2\right)^{7/2}} \tag{1.8}$$

As will be evident in the next sections, it is instructive to break up the integral (1.7) by employing a cutoff parameter Λ and defining the operators

$$\begin{aligned} I_\Lambda\left[h(\kappa)\right]] &\equiv \frac{1}{2\pi^2}\int_0^\Lambda d\kappa\ \kappa^2 h(\kappa)\frac{\sin\kappa\delta}{\kappa\delta} \\ J_\Lambda\left[h(\kappa)\right] &\equiv \frac{1}{2\pi^2}\int_\Lambda^\infty d\kappa\ \kappa^2 h(\kappa)\frac{\sin\kappa\delta}{\kappa\delta} \end{aligned} \tag{1.9}$$

The components of the stress tensor within the wall were computed exactly in [9] for the linear and quadratic walls using (1.5). These correspond to the only values of α for which exact solutions of (1.3) can be expressed in closed-form.

In order to study the Casimir effect under the soft wall model, the renormalized stress tensor should be computed for $\alpha \gg 1$. From (1.1), it is clear that when α is large, the soft wall approximates the Dirichlet wall, under which the Casimir effect was originally derived.

Since the solutions of (1.3) do not have closed-form expressions for $\alpha > 2$, we must approximate $F(z), G(z)$ for all $\kappa \in [0, \infty)$ in order to compute terms of the form (1.7).

In the next section, we develop approximations to the solutions $F(z), G(z)$ of (1.3) for arbitrary values of α. We then use the resulting approximations, together with (1.5) and (5.11) in [9] to compute the renormalized stress tensor inside the cavity for $\alpha = 6$.

2. APPROXIMATING THE GREEN FUNCTION ANALYTICALLY

The task at hand is to generate valid approximations to $g_\kappa(z)$ and $\partial_z^2 g_\kappa(z)$, and therefore to $F(z)$ and $G(z)$, for all $\kappa \in [0, \infty)$. To do this, we generate approximations applicable to various κ regimes. The combination of these approximations yields a piecewise function approximating $F(z)$ and $G(z)$ for all $\kappa > 0$. To verify the correctness this approximation, we generate numerical solutions to (1.3) subject to the boundary conditions (1.4) and compare the results.

2.1 Perturbation Theory

In order to approximate the solutions $F(z), G(z)$ of (1.3), and therefore $g_\kappa(z)$, for small values of κ, we apply perturbation theory to generate their power series expansions. The solutions are approximated by partial sums of these series. Much of the process to obtain the coefficients of these series is described thoroughly in Sec. **III** of [8]. However, only the first order perturbative expansions were computed there, which are insufficient for our purposes.

For the perturbative approximation to be usable as a part of a sufficiently accurate piecewise approximation, it must be carried to a rather high order. This is done by applying (3.12) of [8] and use the natural recursive generalization of (3.8) in [8]

$$\begin{aligned} F_n(z) &= \frac{1}{W(i,k)} \left(k(z) \int_0^z i(a) F_{n-1}(a)\, da + i(z) \int_0^z k(a) F_{n-1}(a)\, da \right) \\ G_n(z) &= \frac{1}{W(i,k)} \left(k(z) \int_0^z i(a) G_{n-1}(a)\, da - i(z) \int_0^z k(a) G_{n-1}(a)\, da \right) \end{aligned} \tag{2.1}$$

where $F_0(z), F_1(z), G_0(z), G_1(z)$ were already computed in [8]. The power series representing the desired solutions are then given by

$$F(z) = \sum_{i=0}^{\infty} F_i(z) \kappa^{2i} \qquad\qquad G(z) = \sum_{i=0}^{\infty} G_i(z) \kappa^{2i} \tag{2.2}$$

The coefficients were evaluated numerically for $2 \leq n \leq 30$, yielding the perturbations $F_{\kappa \ll 1}(z)$ and $G_{\kappa \ll 1}(z)$ of order 30.

The resulting approximation of the Green function for small κ is obtained by plugging them into (1.5)

$$\begin{aligned} g_{\kappa\ll 1}(z) &= F_{\kappa\ll 1}(z)G_{\kappa\ll 1}(z) + \gamma_{\kappa\ll 1}(\kappa)F_{\kappa\ll 1}(z)^2 \\ \gamma_{\kappa\ll 1}(\kappa) &= \frac{1}{\kappa - F'_{\kappa\ll 1}(0)} \end{aligned} \tag{2.3}$$

For accuracy purposes, we do not approximate $\left(\partial_z^2 g_\kappa(z)\right)_{\kappa\ll 1}$ by differentiating (2.3) directly. Instead, we differentiate (1.5) twice and obtain

$$\partial_z^2 g_\kappa(z) = G(z)F''(z) + 2F'(z)G'(z) + 2\gamma(\kappa)\left(F(z)F''(z) + F'(z)^2\right) + F(z)G''(z) \tag{2.4}$$

Since $F(z), G(z)$ are solutions of (1.3), their second derivative is known, and we obtain

$$\begin{aligned} \frac{\left(\partial_z^2 g_\kappa(z)\right)_{\kappa\ll 1}}{2} = F'_{\kappa\ll 1}(z)G'_{\kappa\ll 1}(z) + \gamma_{\kappa\ll 1}(\kappa)\left(F'_{\kappa\ll 1}(z)^2 + F_{\kappa\ll 1}(z)^2\left(\kappa^2 + v(z)\right)\right) + \\ + F_{\kappa\ll 1}(z)G_{\kappa\ll 1}(z)\left(\kappa^2 + v(z)\right) \end{aligned} \tag{2.5}$$

in terms of $F_{\kappa\ll 1}(z), G_{\kappa\ll 1}(z)$ and their first derivatives only.

2.2 The WKB Approximation

For large values of either κ or z, the sought-after solutions are well approximated by an asymptotic series. The WKB approximations of the decaying and growing solutions of (1.3), as well as the dominant part of (1.2), were recorded in (A3) and (A5) in [9] as

$$\begin{aligned} y_\pm(z) &= \frac{e^{\pm\int^z dt[q_0(t)+q_2(t)+q_4(t)+\ldots]}}{\sqrt{q_0(z)+q_2(z)+q_4(z)+\ldots}} \\ \frac{F(z)G(z)}{w} &\approx \frac{1}{2}\frac{1}{q_0(z)+q_2(z)+q_4(z)+\ldots} \end{aligned} \tag{2.6}$$

If we take our basis functions to be

$$\begin{aligned}\hat{F}_{\kappa\gg 1}(z) &= \frac{e^{-\int^z dt[q_0(t)+q_2(t)+q_4(t)+\ldots]}}{\sqrt{q_0(z)+q_2(z)+q_4(z)+\ldots}} \\ \hat{G}_{\kappa\gg 1}(z) &= \frac{e^{+\int^z dt[q_0(t)+q_2(t)+q_4(t)+\ldots]}}{2\sqrt{q_0(z)+q_2(z)+q_4(z)+\ldots}}\end{aligned} \tag{2.7}$$

and compare $\hat{F}_{\kappa\gg 1}(z)\hat{G}_{\kappa\gg 1}(z)$ to (2.6), we immediately conclude that their Wronskian is unity. Since (1.2) holds for any decaying and growing basis functions, plugging in $\hat{F}_{\kappa\gg 1}(z), \hat{G}_{\kappa\gg 1}(z)$ yields:

$$\begin{aligned}g_{\kappa\gg 1}(z) &= \frac{1}{2\left(q_0(z)+q_2(z)+q_4(z)+\ldots\right)} + \frac{\hat{\gamma}(\kappa)e^{-2\int^z dt[q_0(t)+q_2(t)+q_4(t)+\ldots]}}{q_0(z)+q_2(z)+q_4(z)+\ldots} \\ \hat{\gamma}(\kappa) &= \frac{\hat{G}_{\kappa\gg 1}(0)-\hat{G}'_{\kappa\gg 1}(0)/\kappa}{\hat{F}_{\kappa\gg 1}(0)-\hat{F}'_{\kappa\gg 1}(0)/\kappa}\end{aligned} \tag{2.8}$$

As shown in [11], the local functionals q_n may be obtained from a recurrence relation. (In practice, we used a slightly different form of the recursion, found in [12].) The recurrence relation can be solved in a bottom-up manner using dynamic programming. With this approach, the local functionals $q_1, \ldots, q_n$ can be computed in polynomial time.

The first 16 terms were kept in the prefactor of the rational term in (2.8), and the sub-dominant term was taken to have 3 terms in the exponential and two in the prefactor, as in a 4$^{\text{th}}$ order Fröman approximation (see [9] p. 16). The term $\hat{\gamma}(\kappa)$ was then computed by plugging in the 4$^{\text{th}}$ order Fröman approximations of $\hat{F}_{\kappa\gg 1}(z)$ and $\hat{G}_{\kappa\gg 1}(z)$ and taking the limit as $z \to 0$. For computational feasibility, $g_\kappa(z)_{\kappa\gg 1}$ is expanded as an asymptotic series of order 15. The second derivative of the Green function is approximated as

$$\left(\partial_z^2 g_\kappa(z)\right)_{\kappa\gg 1} = \partial_z^2\left(g_\kappa(z)_{\kappa\gg 1}\right) \tag{2.9}$$

2.3 The Intermediate Regime

Equipped with the approximations of the last two sections, we wish to approximate the Green function for values of κ that are too large for the perturbative expansion to be usable, but are not large enough for the WKB approximation to be valid. This process naturally contains arbitrary elements which are rooted in trial and error. These ambiguities are unavoidable, and are ultimately justifiable by the results they yield.

In past attempts, the Green function was approximated by low order perturbative and WKB expansions in the extreme regimes. These approximations were matched by an interpolating spline on the boundary of the intermediate regime.

Another approach, which was tried by Tommy Settlemyre, is to construct a Padé approximant that matches the perturbative and WKB expansions at 0 and ∞ up to a given order. The order of the Padé approximant was chosen to be low enough to yield a pole-free approximant.

While these attempts produced insufficient approximations, they developed ideas that prepared the ground for the method developed here. In this section, we modify these methods and combine them into a sufficiently accurate approximation scheme for the Green function and its second derivative in the intermediate κ regime.

To approximate the Green function in the intermediate κ regime for a fixed $z = z_0$, we pick arbitrary endpoints $\kappa_{L_0}, \kappa_{R_0}, \kappa_{L_2}, \kappa_{R_2}$ for $g_\kappa(z)$ and $\partial_z^2 g_\kappa(z)$, respectively. The interpolating splines will be constructed in the intervals defined by the endpoints. The general form of the splines was chosen to match that of the dominant term in (2.8)

$$g_{\kappa\approx 1}(z_0) = \sum_{i=1}^{n} \frac{A_i}{\kappa^i} \tag{2.10}$$

$$\left(\partial_z^2 g_\kappa(z_0)\right)_{\kappa\approx 1} = \sum_{i=1}^{n} \frac{B_i}{\kappa^i} \tag{2.11}$$

The coefficients $\{A_i\}, \{B_i\}$ were selected to satisfy the conditions (2.12) for all $m = 0, \ldots, \frac{n-2}{2}$

$$\begin{aligned}
\partial_\kappa^m \, g_{\kappa\approx 1}(z_0)\Big|_{\kappa_{L_0}} &= \partial_\kappa^m \, g_{\kappa\ll 1}(z_0)\Big|_{\kappa_{L_0}} & \partial_\kappa^m \left(\partial_z^2 g_\kappa(z_0)\right)_{\kappa\approx 1}\Big|_{\kappa_{L_2}} &= \partial_\kappa^m \left(\partial_z^2 g_\kappa(z_0)\right)_{\kappa\ll 1}\Big|_{\kappa_{L_2}} \\
\partial_\kappa^m \, g_{\kappa\approx 1}(z_0)\Big|_{\kappa_{R_0}} &= \partial_\kappa^m \, g_{\kappa\gg 1}(z_0)\Big|_{\kappa_{R_0}} & \partial_\kappa^m \left(\partial_z^2 g_\kappa(z_0)\right)_{\kappa\approx 1}\Big|_{\kappa_{R_2}} &= \partial_\kappa^m \left(\partial_z^2 g_\kappa(z_0)\right)_{\kappa\gg 1}\Big|_{\kappa_{R_2}}
\end{aligned} \tag{2.12}$$

The endpoints and the order of the splines were chosen by trial and error to make the matrix defining (2.12) as well-conditioned as possible. The endpoints were also chosen to be within the range of validity of their corresponding regime. The spline $g_{\kappa\approx 1}(z_0)$, shown in Fig. 2.1, was constructed using $\kappa_{L_0} = 1.5, \kappa_{R_0} = 9$. The spline $(\partial_z^2 g_\kappa(z_0))_{\kappa\approx 1}$, shown in Fig. 2.2, was constructed using $\kappa_{L_2} = 1.8, \kappa_{R_2} = 12$. Both splines were taken to be of order $n = 10$.

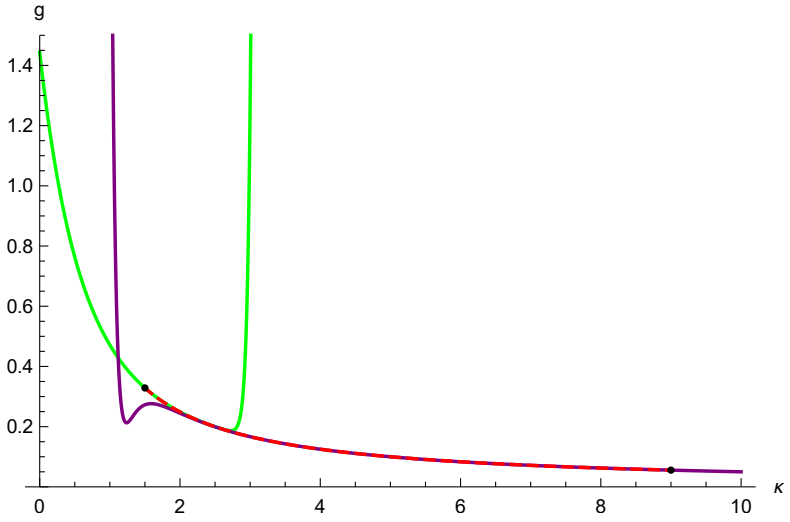

Figure 2.1: The first 31 terms of the perturbative expansion (2.3) (in green), the 15$^{\text{th}}$ order asymptotic series of the first 16 terms of the WKB approximation (2.8) (in purple), and the spline (2.10) (in red dashes) for $\alpha = 6$ and $z = 0.01$. The black dots mark $\kappa_{L_0} = 1.5, \kappa_{R_0} = 9$. The perturbative expansion clearly diverges as κ grows, while the WKB approximation is accurate for moderate values of κ. Since the terms in the WKB series often change sign, the partial sum (in purple) has a "wiggle".

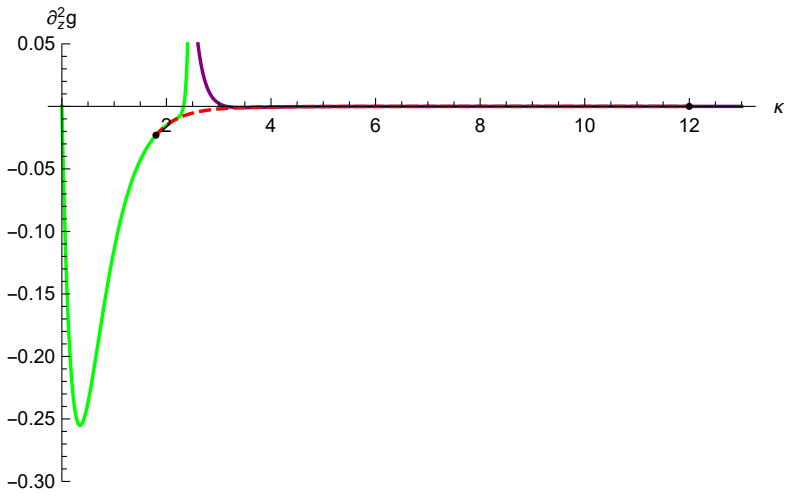

Figure 2.2: The first 31 terms of the perturbative expansion (2.5) (in green), the 15$^{\text{th}}$ order asymptotic series of the first 16 terms of the WKB approximation (2.9) (in purple), and the spline (2.11) for $\alpha = 6$ and $z = 0.01$. The black dots mark $\kappa_{L_2} = 1.8, \kappa_{R_2} = 12$. The perturbative expansion clearly diverges as κ grows, while the WKB approximation is accurate for larger values of κ.

2.4 The Approximated Green Function

As evident in Figs. 2.1 and 2.2, the spline (2.11) spans a larger region than (2.10). Therefore, accuracy issues with the second derivative arise when approximating small quantities such as the pressure. This is resolved by using the approximations (2.4), (2.9) and (2.11) in conjunction with a 2-point Padé approximant.

The 2-point $[\ell/m]$ Padé approximant of a function $f(\kappa)$, as described in [13], is the rational function $P_\ell(\kappa)/Q_m(\kappa)$ whose power series matches $f(\kappa)$ as much as possible at two given points. As shown in Sec. IV of [13], the matching requirements yield linear constraints on the coefficients of $P_\ell(\kappa)$ and $Q_m(\kappa)$. These equations are solved to determine the approximant $P_\ell(\kappa)/Q_m(\kappa)$.

We construct the 2-point $[\ell/m]$ Padé approximant of $\partial_z^2 g_\kappa(z)$ at $\kappa = 0, \infty$ from the perturbation expansion (2.4). Since the Green function behaves as a rational function asymptotically, we may represent it as the series expansion of the dominant term of (2.8) in powers of $1/\kappa$. This series can be differentiated twice with respect to z to yield the asymptotic behavior of $\partial_z^2 g_\kappa(z)$. The Padé approximant will match the behavior of this differentiated series at $\kappa = \infty$.

The Padé approximant of $\partial_z^2 g_\kappa(z)$ will have poles (as a function of κ), near which the other approximations will be used. (Here, "near" was arbitrarily defined to satisfy $|\kappa - \kappa_{pole}| < 0.15$.) Overall, we obtain a piecewise approximation to the Green function and its second derivative

$$\widehat{g}_\kappa(z_0) \equiv \begin{cases} g_\kappa(z_0)_{\kappa \ll 1} & \kappa < \kappa_{L_0} \\ g_\kappa(z_0)_{\kappa \approx 1} & \kappa_{L_0} \leq \kappa \leq \kappa_{R_0} \\ g_\kappa(z_0)_{\kappa \gg 1} & \kappa > \kappa_{R_0} \end{cases}$$

$$|\kappa - \kappa_{pole}| \geq 0.15 \implies \widehat{\partial_z^2\, g}_\kappa(z_0) \equiv [16/16] \text{ Padé approximant of } \partial_z^2 g_\kappa(z) \tag{2.13}$$

$$|\kappa - \kappa_{pole}| < 0.15 \implies \widehat{\partial_z^2\, g}_\kappa(z_0) \equiv \begin{cases} \left(\partial_z^2 g_\kappa(z)\right)_{\kappa \ll 1} & \kappa < \kappa_{L_2} \\ \left(\partial_z^2 g_\kappa(z)\right)_{\kappa \approx 1} & \kappa_{L_2} \leq \kappa \leq \kappa_{R_2} \\ \left(\partial_z^2 g_\kappa(z)\right)_{\kappa \gg 1} & \kappa > \kappa_{R_2} \end{cases}$$

The terms of the form (1.7) are then approximated using the operators (1.9) as

$$\widehat{I}\left[\partial_z^b\ [g - \tilde{g}]\right] \equiv \lim_{\delta \to 0} \left(I_{12}\left[\widehat{\partial_z^b\, g}_\kappa(z)\right] - I_{12}\left[\partial_z^b\, \tilde{g}_\kappa(z)\right] + J_{12}\left[\left(\partial_z^b\, g_\kappa(z)\right)_{\kappa \gg 1} - \partial_z^b\, \tilde{g}_\kappa(z)\right]\right) \tag{2.14}$$

Due to the defined behavior of (2.13) in the large κ region, $\widehat{I}$ is insensitive to the choice of the cutoff parameter, as long as $\Lambda > \kappa_{R_0}, \kappa_{R_2}$. Therefore, we arbitrarily take $\Lambda = 12$.

3. APPROXIMATING THE GREEN FUNCTION NUMERICALLY

3.1 Discretization

To determine the accuracy of the analytical approximation (2.13), we compute the solutions of (1.3) numerically. Since the coefficient multiplying y in (1.3) is unbounded, the differential equation is stiff. This makes the use of ordinary numerical algorithms prone to errors, and therefore unsuitable for our purposes. While specialized stiff numerical solvers exist (such as MATLAB's ode15s), their general-purpose design makes them rather inefficient for our purposes. These solvers are also designed to integrate initial value problems, rendering them useless for finding $F(z)$.

To avoid these issues, we develop a stiff numerical boundary value problem solver tailored to our needs. Unlike general-purpose ODE solvers, our solver will exploit the linearity of (1.3). We discretize the quantities composing (1.3)

$$\vec{z} = \begin{bmatrix} z_0 \\ z_1 \\ \vdots \\ \vdots \\ z_{m+1} \end{bmatrix} \qquad \vec{v} = \begin{bmatrix} v\left(z_0\right) \\ v\left(z_1\right) \\ \vdots \\ \vdots \\ v\left(z_{m+1}\right) \end{bmatrix} \qquad \vec{y} = \begin{bmatrix} y_0 \\ y_1 \\ \vdots \\ \vdots \\ y_{m+1} \end{bmatrix} \qquad \vec{y}_{\text{in}} = \begin{bmatrix} y_1 \\ y_2 \\ \vdots \\ \vdots \\ y_m \end{bmatrix} \tag{3.1}$$

where $v(z)$ is the soft wall of (1.1). We denote the uniform interval width by $h \equiv z_{i+1} - z_i$.

Since the values $y_0,\ y_{m+1}$ are known at the boundary points z_0, z_{m+1}, we solve (1.3) in the domain $[z_1, \cdots, z_m]$. With this goal in mind, we seek a discretization of the differential operator acting on the left hand side of (1.3) which yields m equations for the m unknowns $[y_1, \cdots, y_m]$. The second derivative is approximated by the 6^{th} order centered finite difference formula ([14], [15]) for points sufficiently inside the interval

$$\forall_{\,2\le i\le m-1}: \quad \left.\frac{\partial^2 y}{\partial z^2}\right|_{z_i} \approx \frac{2y_{i-3}-27y_{i-2}+270y_{i-1}-490y_i+270y_{i+1}-27y_{i+2}+2y_{i+1}}{180h^2} \tag{3.2}$$

Although the centered difference approximation is the most accurate, it cannot be used at $z_1,\ z_2,\ z_{m-1},\ z_m$, since these points are not surrounded by 3 other points from both sides. For these points, we use the 6[th] order skewed finite difference formulae ([14], [15])

$$\begin{aligned}
\left.\frac{\partial^2 y}{\partial z^2}\right|_{z_1} &\approx \frac{126y_0-70y_1-486y_2+855y_3-670y_4+324y_5-90y_6+11y_7}{180h^2}\\
\left.\frac{\partial^2 y}{\partial z^2}\right|_{z_2} &\approx \frac{-11y_0+214y_1-378y_2+130y_3+85y_4-54y_5+16y_6-2y_7}{180h^2}\\
\left.\frac{\partial^2 y}{\partial z^2}\right|_{z_{m-1}} &\approx \frac{[-2,16,-54,85,130,-378,214,-11]\cdot[y_{m-6},y_{m-5},\ldots,y_m,y_{m+1}]}{180h^2}\\
\left.\frac{\partial^2 y}{\partial z^2}\right|_{z_m} &\approx \frac{[11,-90,324,-670,855,-486,-70,126]\cdot[y_{m-6},y_{m-5},\ldots,y_m,y_{m+1}]}{180h^2}
\end{aligned} \tag{3.3}$$

The portion of the operators (3.2), (3.3) independent of the boundary conditions $y_0,\ y_{m+1}$ can be combined into the $m\times m$ matrix

$$D_z^2 = \frac{1}{180h^2}\begin{bmatrix}
-70 & -486 & 855 & -670 & 324 & -90 & 11 & 0 & \cdots & 0\\
214 & -378 & 130 & 85 & -54 & 16 & -2 & 0 & \cdots & 0\\
-27 & 270 & -490 & 270 & -27 & 2 & 0 & 0 & \cdots & 0\\
2 & -27 & 270 & -490 & 270 & -27 & 2 & 0 & \cdots & 0\\
0 & 2 & -27 & 270 & -490 & 270 & -27 & 2 & \cdots & \vdots\\
\vdots & & \ddots & \ddots & \ddots & \ddots & \ddots & \ddots & \ddots & \vdots\\
\vdots & & & \ddots & \ddots & \ddots & \ddots & \ddots & \vdots & \\
0 & \cdots & 0 & 0 & 2 & -27 & 270 & -490 & 270 & -27\\
0 & \cdots & 0 & -2 & 16 & -54 & 85 & 130 & -378 & 214\\
0 & \cdots & 0 & 11 & -90 & 324 & -670 & 855 & -486 & -70
\end{bmatrix} \tag{3.4}$$

The matrix (3.4) can fully represent the finite difference operators by adding the appropriate boundary terms to the elements corresponding to the second derivative at $z_1, z_2, z_3, z_{m-2}, z_{m-1}, z_m$.

This is easily done by adding a constant vector to (3.4)

$$\forall_{\,1\le i\le m}: \quad \left.\frac{\partial^2 y}{\partial z^2}\right|_{z=z_i} = \left(D_z^2\,\vec{y}_{\text{in}} + \vec{b}\right)_i + O(h^6)$$

$$\vec{b} = \frac{1}{180h^2}\begin{bmatrix} 126y_0 \\ -11y_0 \\ 2y_0 \\ 0 \\ \vdots \\ 0 \\ 2y_{m+1} \\ -11y_{m+1} \\ 126y_{m+1} \end{bmatrix} \tag{3.5}$$

Denoting $A_m \equiv -D_z^2 + \mathrm{diag}(\vec{v})$, we discretize (1.3) as

$$\underbrace{\left(A_m + \kappa^2 I_{m\times m}\right)}_{\mathcal{L}_m}\vec{y}_{\text{in}} = \vec{b} \tag{3.6}$$

Since the rows of $\mathcal{L}_m$ correspond to conditions on the solution at distinct points, they are linearly independent, and $\mathcal{L}_m$ is nonsingular. Therefore, the boundary conditions $y_0,\ y_{m+1}$ (which define $\vec{b}$) uniquely determine the solution of (3.6), as intended.

After the solutions F, G are computed, the numerical Green function $g_{\text{num}}(z)$ is immediately obtained from (1.5). In order to use (2.4) and compute $\partial_z^2 g_{\text{num}}(z)$, we will compute F', G', and repeat the procedure of (2.5). The first derivatives are computed from the appropriate centered and skewed 6$^{\text{th}}$ order finite difference formulae (see [14], [15]).

3.2 Boundary Conditions

To solve for $F(z)$, we approximate the decaying behavior by taking a sufficiently large value of z_{m+1}, and demanding that $F(z_{m+1})$ effectively vanishes. Using (2.7), we conclude that $z_{m+1} = 10$ can be taken to be the interval endpoint for our purposes.

Since both conditions for $G(z)$ in (1.4) are given at $z = 0$, we cannot solve for it using (3.6) directly. However, we can solve a related boundary value problem, obtain the solution $\overline{G}$, and deduce $G(z)$ from it. Since $G(z)$ is defined to be exponentially increasing, we enforce the boundary condition $\overline{G}(0) = G(0) = 0$, and guess a larger boundary condition for $\overline{G}$ at a reasonable endpoint z_{m+1}, as shown in Table 3.1. The function $\frac{\overline{G}(z)}{\overline{G}'(0)}$ clearly satisfies the initial conditions in (1.4), and must coincide with $G(z)$ from uniqueness arguments.

Table 3.1: Summary of the boundary conditions used to solve (3.6).

function	z_0	y_0	z_{m+1}	y_{m+1}
F	0	1	10	0
$\overline{G}$	0	0	2	1

3.3 Solution Techniques

So far, we assumed that κ is fixed, and developed a method to solve for the basis functions $F(z), G(z)$. Since our goal is to compute integrals of the type $I_\Lambda[g]$, which are defined in (1.9), the process described above must be repeated for all values $\kappa \in \mathbf{K} \equiv \{\kappa_1, \ldots, \kappa_n\}$ in the desired range. The size of the range, n, depends on the cutoff parameter Λ and the desired interval width $\Delta\kappa$. These parameters directly affect the accuracy of of the numerical integration.

Naively, the system (3.6) can be solved by banded Gaussian elimination for all $\kappa \in \mathbf{K}$ in $O(nm)$, since $bandwidth \ll m$ (see [16] p. 177). In this section, we develop two alternative approaches that take the special properties of $\mathcal{L}_m$ into account, and analyze their performance.

3.3.1 Solution by Eigenvalue Decomposition

A key property of (3.6) is that $\mathcal{L}_m$ is obtained from a κ-dependent diagonal shift of the fixed diagonalizable operator A_m. In situations where n is sufficiently large, it becomes economical to solve the system by computing its eigenvalue decomposition. Such decomposition allows us to obtain solutions for (3.6) by matrix multiplications alone. When n is large, the matrices involved can be multiplied efficiently using a GPU device.

Once we compute the eigenvalue decomposition $A_m = VDV^{-1}$, the inverse of a diagonal shift by κ^2 is easily obtained as

$$\mathcal{L}_m^{-1} = \left(A_m + \kappa^2 I_{m\times m}\right)^{-1} = \left(V\left(D + \kappa^2 I_{m\times m}\right)V^{-1}\right)^{-1} = V\left(D + \kappa^2 I_{m\times m}\right)^{-1}V^{-1} \tag{3.7}$$

The inverse of the shifted diagonal matrix is obtained by taking the reciprocals of its diagonal entries, which is easily done in $O(m)$.

By pre-computing the eigenvalue decomposition VDV^{-1} of A_m and the vector $V^{-1}\vec{b}$, the system (3.6) can be solved by an element-wise vector multiplication, followed by a matrix multiplication. Parallelizing these operations yields the following algorithm:

Algorithm 1: Solution by Eigenvalue Decomposition

Data: The wall stiffness, the size of the system, the boundary conditions, and the κ range

Result: The discrete solution $y(\kappa, z) \in \mathbb{R}^{n\times(m+2)}$ of (3.6) and its first derivative

initialize $\vec{b}$ according to (3.5)

initialize D_z^2 according to (3.4)

$\vec{z} \leftarrow$ **linspace**$(z_0, z_{m+1}, m+2)$

$h \leftarrow z_2 - z_1$

$\forall_{1\le i\le m}\ (\vec{v})_i \leftarrow (z_i)^\alpha$ `// Element-wise power`

$A_m \leftarrow -D_z^2 + \mathrm{diag}(\vec{v})$

$V, \vec{d} \leftarrow$ **eig**(A_m) `//` $A_m = V\,\mathrm{diag}\left(\vec{d}\right) V^{-1}$

$\vec{u} \leftarrow V^{-1}\vec{b}$

transfer $V, \vec{d}, \vec{u}$, and $\mathbf{K}$ to the GPU device as sparse arrays

$(shifts^{-1})_{ij} \leftarrow \left(d_i + \kappa_j^2\right)^{-1}$ `//` $shifts^{-1}$ `is the matrix containing the reciprocal of the shifts of the eigenvalues` $\vec{d}$ `by` κ_j^2 `for all` $\kappa_j \in \mathbf{K}$

$\left(u_{shifts^{-1}}\right)_{ij} \leftarrow (\vec{u})_i \left(shifts^{-1}\right)_{ij}$ `// The` j^{th} `column of` $u_{shifts^{-1}}$ `is the vector` $\left(\mathrm{diag}\left(\vec{d}\right) + \kappa_j^2 I_{m\times m}\right)^{-1}\vec{u}$.

$y \leftarrow$ **pagefun**$(\times, V, u_{shifts^{-1}})$ `// Multiply the matrices in parallel`

add a column of y_0's to the left and a column of y_{m+1}'s to the right of y

obtain y' from the appropriate 6^{th} order finite difference formulae

The algorithm above was implemented in MATLAB and executed on a single 28-core GPU compute node of the HPRC machine Terra. According to [17], each of Terra's 48 GPU compute nodes has two Intel Xeon E5-2680 v4 2.40GHz 14-core processors, one NVIDIA K80 Accelerator, and 128 GB of RAM. All of Terra's nodes are connected by an Intel OPA-based interconnect.

To solve for F, G, we use the stiffness $\alpha = 6$ and the boundary conditions in Table 3.1. To obtain an interval width of $h = 10^{-3}$, we solve for F with $m_F = 9999$, and G with $m_G = 1999$.

3.3.2 *Low Rank Updates to Symmetric Matrices*

Another nontrivial approach to solve (3.6) is to decompose $\mathcal{L}_m$ into a sum of a symmetric positive definite matrix S_m and corrections. This decomposition allows us to solve the system $(S_m + \kappa^2 I_{m\times m})\,\vec{y}_{\text{in}} = \vec{b}$ without pivoting (see [16] p. 180). Since A_m is nearly symmetric, we decompose it into a symmetric matrix and a rank-8 correction

$$
\begin{aligned}
&A_m = S_m + UV^\top \qquad \text{where } S_m \text{ is symmetric positive definite and}\\
&U,V \in \mathbb{R}^{m\times 8} \qquad \text{have columns}\\
&\vec{u_1} = \hat{\mathbf{e}}_{\mathbf{1}}, \quad \vec{v_1} = \frac{1}{180h^2}[0,\ 486,\ -855,\ 670,\ -324,\ 90,\ -11,\ 0\dots 0]\\
&\vec{u_2} = \hat{\mathbf{e}}_{\mathbf{2}}, \quad \vec{v_2} = \frac{1}{180h^2}[-214,\ 0,\ -130,\ -85,\ 54,\ -16,\ 2,\ 0\dots 0]\\
&\vec{u_3} = \frac{1}{180h^2}[0,\ 0,\ 27,\ -2,\ 0\dots 0], \quad \vec{v_3} = \hat{\mathbf{e}}_{\mathbf{1}}\\
&\vec{u_4} = \frac{1}{180h^2}[0,\ 0,\ -270,\ 27,\ -2,\ 0\dots 0], \quad \vec{v_4} = \hat{\mathbf{e}}_{\mathbf{2}}\\
&\vec{u_5} = \frac{1}{180h^2}[0\dots 0,\ -2,\ 27,\ -270,\ 0,\ 0], \quad \vec{v_5} = \hat{\mathbf{e}}_{\mathbf{m-1}}\\
&\vec{u_6} = \frac{1}{180h^2}[0\dots 0,\ -2,\ 27,\ 0,\ 0], \quad \vec{v_6} = \hat{\mathbf{e}}_{\mathbf{m}}\\
&\vec{u_7} = \hat{\mathbf{e}}_{\mathbf{m-1}}, \quad \vec{v_7} = \frac{1}{180h^2}[0\dots 0,\ 2,\ -16,\ 54,\ -85,\ -130,\ 0,\ -214]\\
&\vec{u_8} = \hat{\mathbf{e}}_{\mathbf{m}}, \quad \vec{v_8} = \frac{1}{180h^2}[0\dots 0,\ -11,\ 90,\ -324,\ 670,\ -855,\ 486,\ 0]
\end{aligned}
\tag{3.8}
$$

To solve (3.6), the solution $\mathcal{L}_m^{-1}\vec{b}$ should be expressed in terms of $S_m^{-1}\vec{b}$, the diagonal shift $\kappa^2 I_{m\times m}$, and the rank-8 updates defined in (3.8). To do this, we use the Sherman-Morrison-Woodbury formula for $\mathcal{L}_m$ (see [16] p. 65)

$$
\begin{aligned}
&\mathcal{L}_m^{-1}\vec{b} = \left(T_m + UV^\top\right)^{-1}\vec{b} = T_m^{-1}\vec{b} - T_m^{-1}U\underbrace{\left(I_{8\times 8} + V^\top T_m^{-1}U\right)^{-1}}_{M_8}V^\top T_m^{-1}\vec{b}\\
&T_m \equiv S_m + \kappa^2 I_{m\times m}
\end{aligned}
\tag{3.9}
$$

The representation (3.9) reduces the computation to one that requires an 8×8 Gaussian elimination and inversions of T_m, which is symmetric positive definite. The former takes $O(1)$

time, while the latter is easily done by a band Cholesky algorithm in $O(m)$, which does not require pivoting (see [16] p. 180). Since no pivoting is performed in the band Cholesky algorithm, it is instructive to reverse the order in which we solve for $G(z)$. Since $G(z)$ is exponentially increasing, we reorder the unknowns $\vec{y}_{\text{in}}$ and the domain $\vec{z}$ descendingly. The reversal results in the largest diagonal elements of A_m occurring at its beginning, yielding a more stable factorization.

Another way to compute the inversions T_m^{-1} efficiently is to use the eigenvalue decomposition method shown in the last subsection. Since S_m is symmetric, its eigenvalue decomposition is faster to compute than $\mathcal{L}_m$'s. Similarly to algorithm 1, the inversions in (3.9) reduce to matrix multiplications, which can easily be executed in parallel. While our initial implementation of this process is not competitive, a more thoughtful implementation may improve its performance significantly.

The use of (3.9) and Cholesky factorization is numerically stable and produces extremely accurate results. Since our goal is to compute the weighted integrals (1.9), numerical accuracy is essential. For our purposes and for other applications which prioritize accuracy, the following is preferable to algorithm 1:

Algorithm 2: Solution by the Sherman-Morrison-Woodbury formula

Data: The wall stiffness, the size of the system, the boundary conditions, and the κ range

Result: The discrete solution $y(\kappa, z) \in \mathbb{R}^{n\times(m+2)}$ of (3.6) and its first derivative

initialize $\vec{b}$ according to (3.5)

initialize D_z^2 according to (3.4)

$\vec{z} \leftarrow$ **linspace**$(z_0, z_{m+1}, m+2)$

$h \leftarrow z_2 - z_1$

reverse the order of $\vec{b}, \vec{z}$ if solving for $G(z)$

$\forall_{1\le i\le m}\ (\vec{v})_i \leftarrow (z_i)^\alpha$ `// Element-wise power`

$A_m \leftarrow -D_z^2 + \mathrm{diag}(\vec{v})$

initialize S_m, U, V according to (3.8)

forall $\kappa \in$ K ***concurrently*** **do**

$R \leftarrow$ **chol** (S_m) `//` $S_m + \kappa^2 I_{m\times m} = R^\top R$`, where` R `is an upper triangular matrix`

$\vec{x} \leftarrow R\backslash\left(R^\top\backslash\vec{b}\right)$ `// the operation \ solves the linear system using forward and backward substitutions`

$M_8 \leftarrow I_{8\times 8} + V\left(R\backslash\left(R^\top\backslash U\right)\right)$ `//` see (3.9)

$solution \leftarrow \vec{x} - R\backslash\left(R^\top\backslash\left(UM_8\backslash\left(V\vec{x}\right)\right)\right)$

$y(\kappa, :) \leftarrow [y_0,\ solution,\ y_{m+1}]$

end

revert $\vec{b}, \vec{z}, y(\kappa, :)$ back to the original order if solving for $G(z)$

obtain y' from the appropriate 6th order finite difference formulae

Algorithm 2 was implemented in MATLAB and executed on a single 28-core Terra compute node with the same input fed into algorithm 1. According to [17], each of Terra's 256 general compute nodes has two Intel Xeon E5-2680 v4 2.40GHz 14-core processors and 64 GB of RAM.

Fig. 3.1 shows the performance of both algorithms as a function of n, excluding the cost of the eigendecomposition. Figs. 3.2-3.4 show the runtime, speedup, and efficiency of algorithm 2.

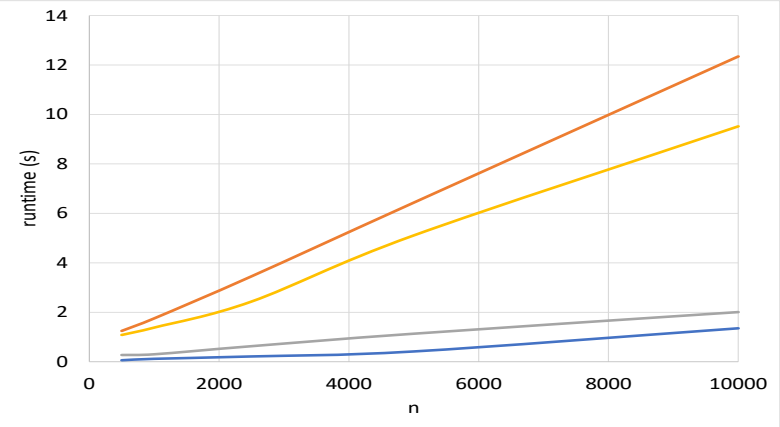

Figure 3.1: The running times of algorithm 1 for F, algorithm 2 for F, algorithm 2 for G, and algorithm 1 for G, from top to bottom. The parallel loop in algorithm 2 was executed with 12 worker threads.

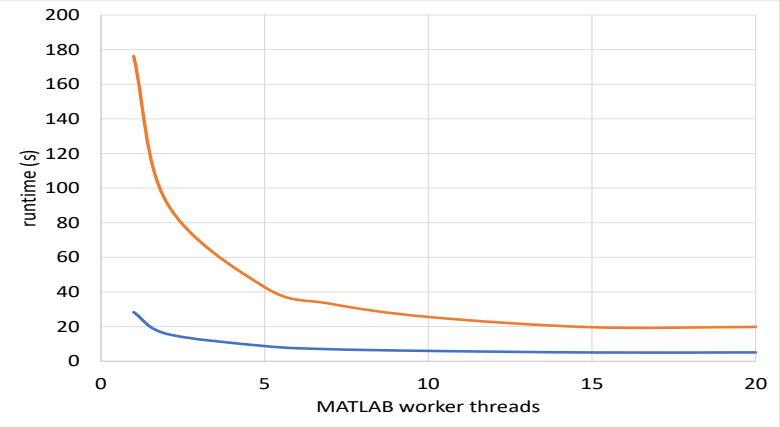

Figure 3.2: The runtime of algorithm 2 for G (in blue) and F (in orange) as a function of the number of worker threads for $n = 25000$

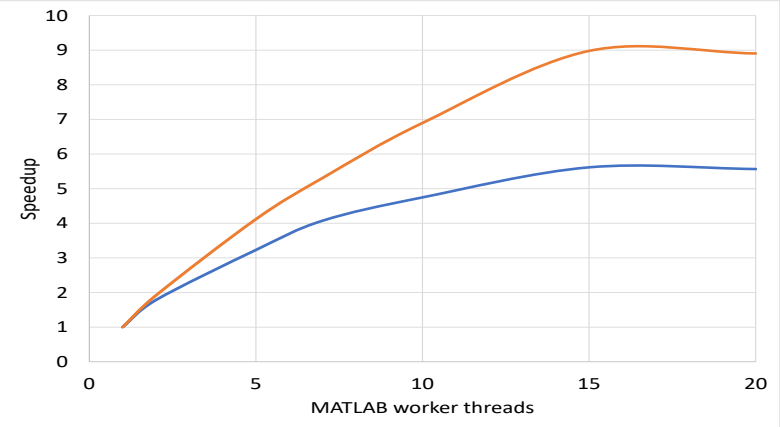

Figure 3.3: The speedup of algorithm 2 for G (in blue) and F (in orange) as a function of the number of worker threads for $n = 25000$

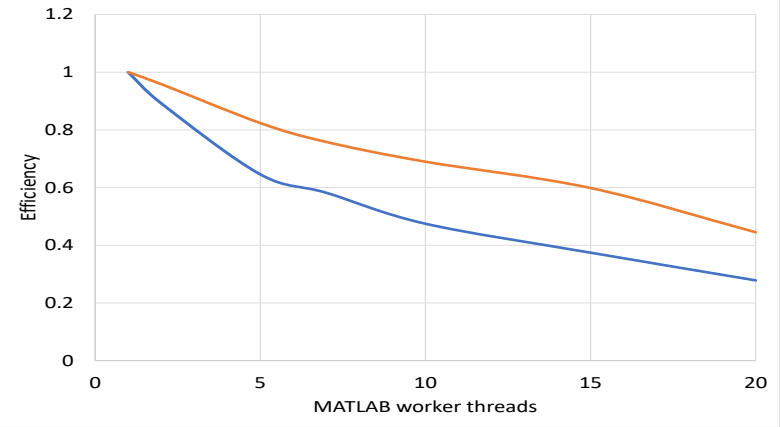

Figure 3.4: The efficiency of algorithm 2 for G (in blue) and F (in orange) as a function of the number of worker threads for $n = 25000$

3.4 The Numerical Green Function

The resulting solution is well behaved for moderate values of κ, after which it becomes increasingly inaccurate. This behavior is expected, since (1.3) is stiff, and the error introduced by the finite difference approximation grows polynomially in κ.

For accuracy purposes, the solutions F, G were obtained from algorithm 2 with $n = 25000$ and the same parameters as before, namely $m_F = 9999, m_G = 1999$. The Green function and its second derivative, displayed in Figs. 3.5 and 3.6, were computed from these basis functions according to (1.5) and the equivalent of (2.5).

The terms in (1.7) are computed numerically using the numerical counterpart of (2.14)

$$I_{\text{num}}\left[\partial_z^b\ [g-\tilde{g}]\right] \equiv \lim_{\delta\to 0}\left(I_{25}\left[\partial_z^b\ g_{\text{num}}(z)\right] - I_{25}\left[\partial_z^b\ \tilde{g}_\kappa(z)\right] + J_{25}\left[\left(\partial_z^b\ g_\kappa(z)\right)_{\kappa\gg 1} - \partial_z^b\ \tilde{g}_\kappa(z)\right]\right) \tag{3.10}$$

Since the numerical Green function is discrete, the integrals in (3.10) are evaluated by integrating an interpolating cubic spline over κ for each value of z. The cutoff parameter $\Lambda = 25$ reflects the region where the numerical solution is valid. For values slightly larger than $\kappa = 25$, the second derivative of the Green function starts decreasing. Although minuscule, this behavior is undesirable and disagrees with the expected qualitative behavior of g''.

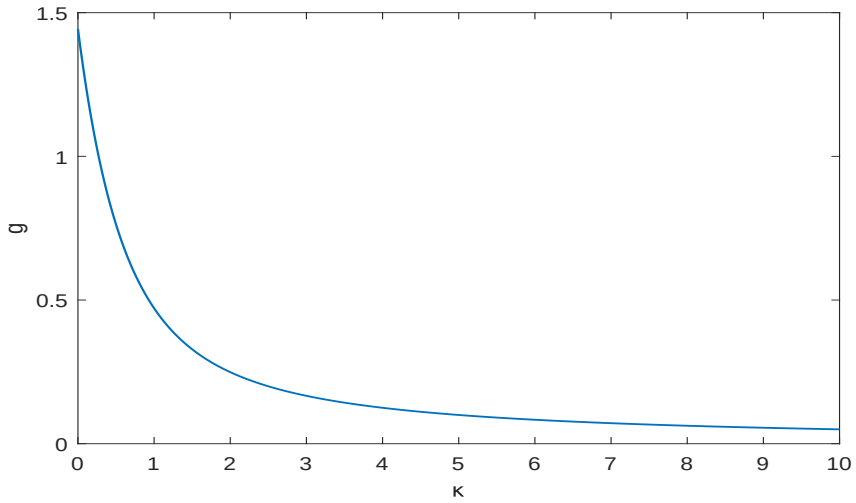

Figure 3.5: The numerical Green function obtained from algorithm 2 for $\alpha = 6$ and $z = 0.01$.

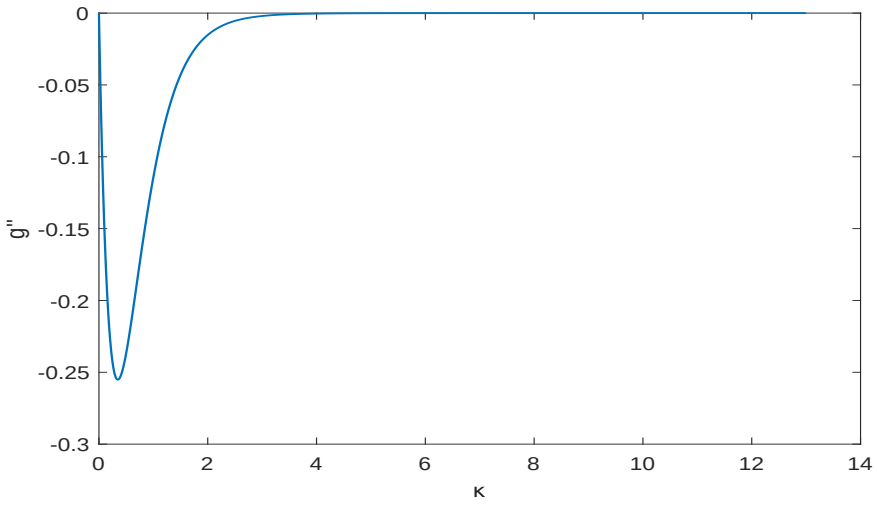

Figure 3.6: The second derivative of the numerical Green function obtained from algorithm 2 for $\alpha = 6$ and $z = 0.01$. To minimize numerical error, g'' was calculated from the basis functions and their first derivatives similarly to (2.5).

4. APPROXIMATING THE STRESS TENSOR

Using the scheme developed in the last section and equation (5.11) in [9], we approximate the stress tensor components for $\alpha = 6$ within the wall. The mass scale μ is taken to be 1.

4.1 The Energy Density

Following the notation introduced in [8], we define $\beta \equiv \xi - \frac{1}{4}$, where ξ is the conformal parameter. Plugging the soft wall (1.1) into (5.11) of [9] yields

$$\begin{aligned}\left\langle T^{00}\right\rangle_R = &\frac{-\alpha z^{\alpha+2}\left(\alpha(48\beta+3)+2(\alpha-1)(12\beta+1)\log\left(z^\alpha\right)-24\beta-2\right)}{384\pi^2 z^4} \\ &+\frac{12(\alpha-2)\alpha\beta+3z^{2\alpha+4}\left(2\log\left(z^\alpha\right)-1\right)}{384\pi^2 z^4}+\left\langle T^{00}\right\rangle\left[I\left[g-\tilde{g}\right]\right]\end{aligned} \tag{4.1}$$

where the last term is given by (6.3) in [9] as

$$\left\langle T^{00}\right\rangle\left[I\left[g-\tilde{g}\right]\right] = -\left(I\left[\frac{\kappa^2}{3}\left[g-\tilde{g}\right]\right]+I\left[\beta\partial_z^2\left[g-\tilde{g}\right]\right]\right) \tag{4.2}$$

We compute this term using $\widehat{I}$ and I_{num} defined in (2.14) and (3.10) respectively.

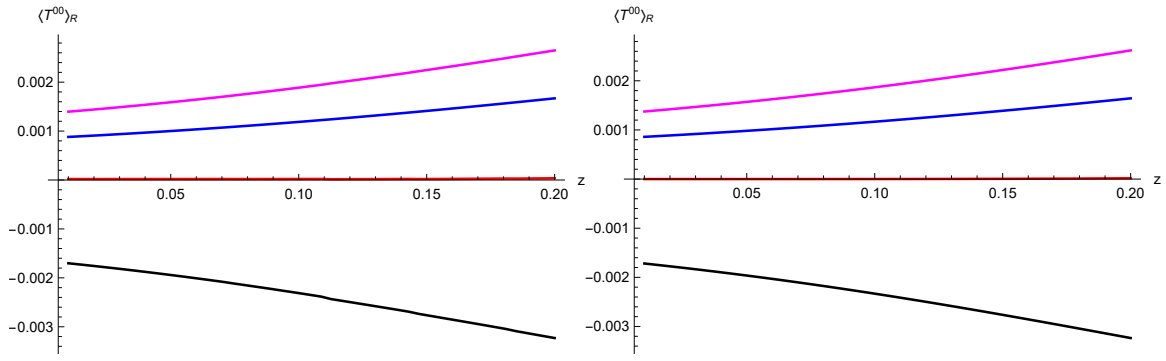

(a) (b)

Figure 4.1: (a) The approximated energy density within the sextic wall obtained from $\widehat{I}$.
(b) The numerical energy density within the sextic wall from I_{num}.
The curves show $\beta = 1/20, 0, -1/12, -1/4$, from top to bottom.

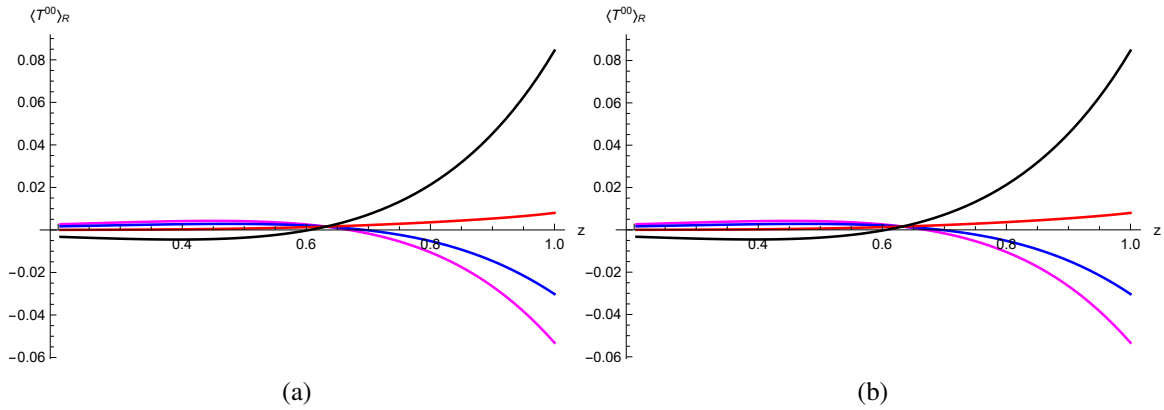

Figure 4.2: (a) The approximated energy density within the sextic wall for large z.
(b) The numerical energy density within the sextic wall for large z.
The energy density clearly changes signs in the large z region.

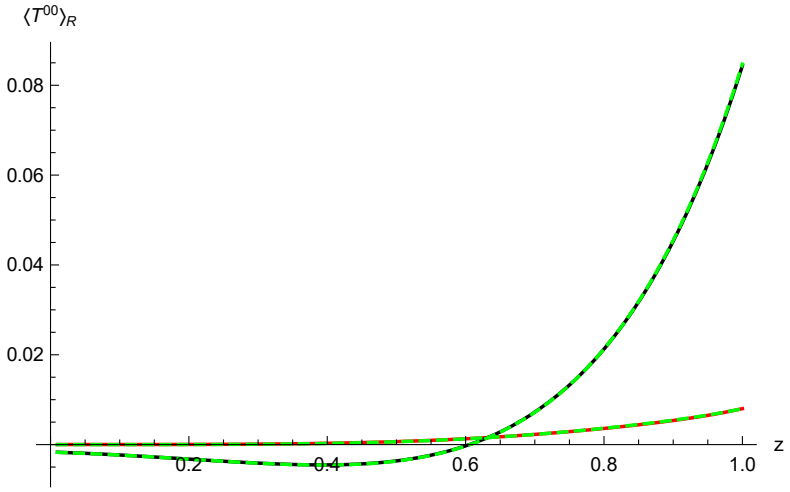

Figure 4.3: The approximated energy density for the minimally coupled case ($\beta = -1/4$, in black) and the conformal case for $\alpha = 6$. The dashed green curves are the corresponding numerical energy densities.

To evaluate (4.1), the integrals defining $\widehat{I}$ and I_{num} were evaluated numerically. The resulting energy density in the small and large z regions is shown in Figs. 4.1 and 4.2. Fig. 4.3 further illustrates the consistency of the approximation and the numerical calculations.

4.2 The Pressure

Similarly to the energy density, (5.11) in [9] reads

$$\langle T^{zz}\rangle_R = \frac{\alpha^2 z^{\alpha+2} - 3z^{2\alpha+4}\left(2\log\left(z^\alpha\right) - 1\right) - 3(\alpha-2)\alpha}{384\pi^2 z^4} + \langle T^{zz}\rangle\left[I\left[g-\tilde{g}\right]\right] \tag{4.3}$$

where the last term is given by (2.13d) in [9] as

$$\langle T^{zz}\rangle\left[I\left[g-\tilde{g}\right]\right] = I\left[\frac{1}{4}\partial_z^2\left[g-\tilde{g}\right]\right] - I\left[\left(\kappa^2 + z^\alpha\right)\left[g-\tilde{g}\right]\right] \tag{4.4}$$

and is again computed using $\widehat{I}$ and I_{num}. As before, the integrals defining $\widehat{I}$ and I_{num} were evaluated numerically.

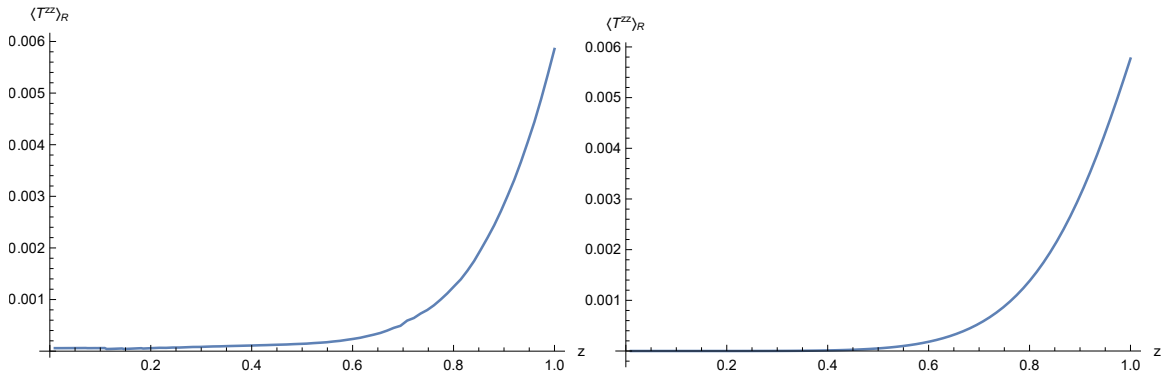

(a) (b)

Figure 4.4: (a) The approximated pressure within the sextic wall obtained from $\widehat{I}$.
The approximated pressure for small z is dominated by the error introduced by the spline in (2.13).
(b) The numerical pressure within the sextic wall obtained from I_{num}.

As evident in Fig. 4.4, the approximated pressure is inaccurate in the small z regime, despite being numerically small. Had the range of Fig. 4.4 been restricted to that of Fig. 4.1, the curves would seem drastically different. In this region, the pressure is significantly smaller than the typical error of (2.13), rendering its accurate computation unfeasible.

4.3 Conservation Laws

Since the trace and divergence identities associated with $\langle T^{\mu\nu} \rangle_R$ depend on the vacuum expectation value of ϕ^2, its renormalization must be consistent with the renormalization of the stress tensor.

In order to avoid a "blow up" at the origin, $\langle \phi^2 \rangle$ was renormalized as

$$\left\langle \phi^2 \right\rangle_R = I_R \left[g_\kappa(z) \right] \equiv I \left[g_\kappa(z) - g_\kappa^{(0)}(z) \right] + \frac{z^\alpha \log\left(z^\alpha\right)}{16\pi^2} \tag{4.5}$$

where $g_\kappa^{(0)}(z) = \frac{1}{2\sqrt{z^\alpha + \kappa^2}}$ is the zeroth order WKB approximation of the Green function, and the last term is obtained from the like order terms in (5.2) in [9].

This renormalization allows us to verify the trace identity (shown in Fig. 4.5) and the divergence identity (shown in Fig. 4.6). Since the stress tensor is independent of other coordinates, $\partial_\mu \langle T^{\mu\nu} \rangle_R = \partial_z \langle T^{zz} \rangle_R$, and the divergence is the derivative of the pressure shown in Fig. 4.4.

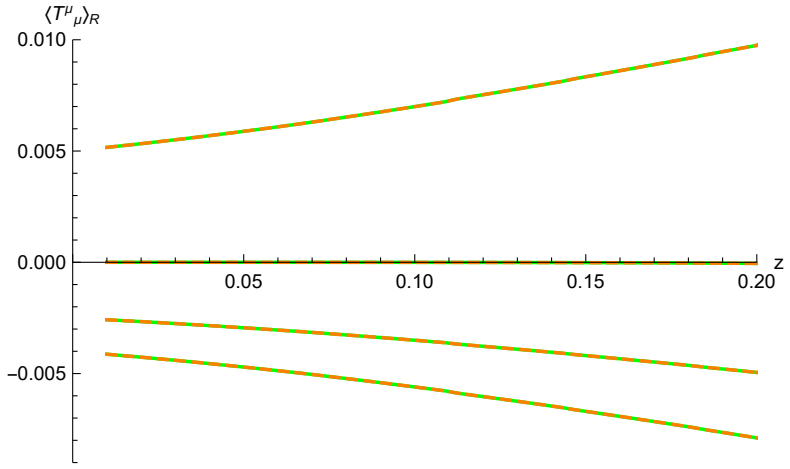

Figure 4.5: The approximated trace (in green) and the trace anomaly identity (5.10) in [9] with $I_R \mapsto \widehat{I}_R$ (in orange dashes) for $\alpha = 6$. The curves show $\beta = 1/20, 0, -1/12, -1/4$, from bottom to top. The curves overlap since the equation holds.

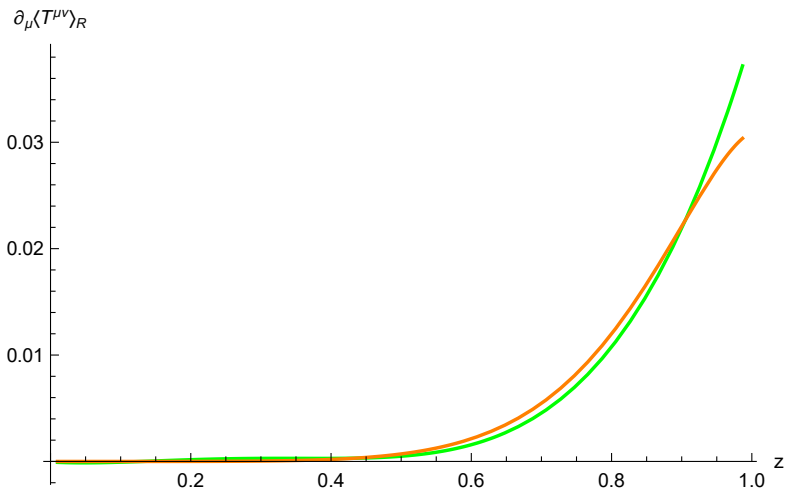

Figure 4.6: The approximated divergence (in green) and $-\widehat{I}_R v'/2$ (in orange) for $\alpha = 6$. According to (5.8) in [9], the curves should coincide. Since the approximated pressure plot is not smooth, its derivative was computed by fitting Fig. 4.4(a) into a polynomial of degree $\alpha - 1$.

4.4 Reproducing the Energy Density for the Quadratic Wall

In order to further verify the approximation (2.13), we reproduce the energy density for the quadratic wall, which was computed from the exact Green function in [9]. Since the quadratic wall is significantly "softer" than the sextic wall, the perturbations (2.3), (2.4) and the WKB approximations (2.8), (2.9) are much closer to each other than shown in Figs. 2.1 and 2.2. Therefore, the endpoints were chosen to be closer together ($\kappa_{L_0} = \kappa_{L_2} = 1, \kappa_{R_0} = \kappa_{R_2} = 2.5$).

While the proximity of the endpoints makes the equations for the coefficients of the Padé approximant underdetermined, it reduces the error of the splines significantly, making the use of a Padé approximant unnecessary. Therefore, for the purpose of verifying the methodologies developed in this paper, we omit the Padé approximant from (2.13). Using the approximated Green function for the quadratic wall, the energy density was calculated from (4.1) and (4.2) as before.

For comparison purposes, the data associated with Fig. 4 in [9] was obtained from the authors. Fig. 4.7 clearly demonstrates the consistency of our approximation with the calculation conducted in [9].

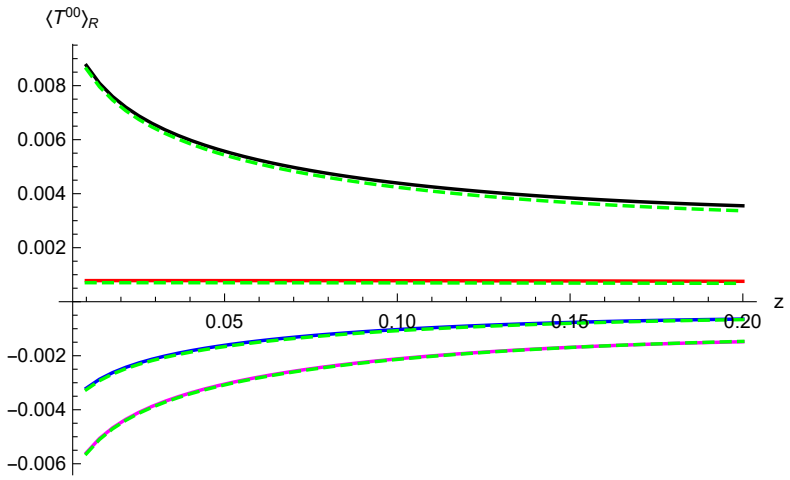

Figure 4.7: The approximated energy density for $\alpha = 2$ obtained from $\widehat{I}$
for $\beta = 1/20, 0, -1/12, -1/4$, from bottom to top (in solid curves).
The dashed green curves are the corresponding energy densities from the data of Fig. 4 in [9].

5. CONCLUSION

The methodologies developed in this paper successfully generalize the analysis and results given in [9] to arbitrarily "hard" power walls. Using high order perturbative and WKB expansions, we approximated the Green function and its relevant derivatives to high accuracy in the small and large κ regimes.

These approximations were used to interpolate the functions in the intermediate regime. By constructing a spline that matches the perturbative and WKB expansions at the appropriate endpoints, we obtained piecewise analytical approximations to the Green function and its second derivative. These approximations were then used to compute the renormalized stress tensor inside the sextic wall.

To validate the approximated results, we compared them to their numerical counterparts. The numerical approximations were obtained by discretizing the equation of motion of the scalar field ϕ and solving the resulting matrix equation. The solution process was optimized by utilizing techniques of numerical linear algebra and parallel computing.

As evident in this work, the approximated stress tensor agrees with its numerical counterpart, indicating its validity. Furthermore, as expected of a consistent approximation scheme, the approximated stress tensor also satisfies the renormalized trace and divergence identities. To further assert the validity of the scheme, we reproduced the energy density for the quadratic wall, which was computed in [9]. Our results agree with the results in Fig. [4] of [9] within reasonable error.

In future work, we hope to generalize and improve the approximation method in the intermediate κ regime. The current method relies on many arbitrary elements, and may not be valid for arbitrary values of z. Since the construction of the interpolating spline is the main source of error in our piecewise approximation, its computation under a more robust scheme will decrease the discrepancies between the analytical and numerical results.

REFERENCES

[1] H. B. G. Casimir, "On the attraction between two perfectly conducting plates," *Proc. Kon. Ned. Akad. Wet.*, vol. **51**, pp. 793–795, 1948.

[2] M. Fierz, "Zur anziehung leitender ebenen im vakuum," *Helv. Phys. Acta*, vol. **33**, pp. 855–858, 1960.

[3] T. H. Boyer, "Quantum zero-point energy and long-range forces," *Ann. Phys.*, vol. **56**, pp. 474–503, 1970.

[4] C. M. Bender and P. Hays, "Zero-point energy of fields in a finite volume," *Phys. Rev. D*, vol. **14**, p. 2622–2632, 1976.

[5] R. Estrada, S. A. Fulling, and F. D. Mera, "Surface vacuum energy in cutoff models: pressure anomaly and distributional gravitational limit," *Journal of Physics A: Mathematical and Theoretical*, vol. **45**, no. 45, p. 455402, 2012.

[6] J. Bouas, S. Fulling, F. Mera, K. Thapa, C. Trendafilova, and J. Wagner, "Investigating the spectral geometry of a soft wall," in *Proc. Symp. Pure Math* (A. H. B. et al, ed.), no. 84, pp. 139–154, 2012.

[7] K. A. Milton, "Hard and soft walls," *Physical Review D*, vol. **84**, p. 065028, 2011.

[8] S. Murray, C. Whisler, S. Fulling, J. Wagner, H. Carter, D. Lujan, F. Mera, and T. Settlemyre, "Vacuum energy density and pressure near a soft wall," *Physical Review D*, vol. **93**, no. 10, p. 105010, 2016.

[9] K. A. Milton, S. A. Fulling, P. Parashar, P. Kalauni, and T. Murphy, "Stress tensor for a scalar field in a spatially varying background potential: Divergences, "renormalization", anomalies, and Casimir forces," *Physical Review D*, vol. **93**, no. 8, p. 085017, 2016.

[10] S. A. Fulling, T. E. Settlemyre, and K. A. Milton, "Renormalization for a scalar field in an external scalar potential," *Symmetry*, vol. **10**, no. 3, 2018.

[11] J. Campbell, "Computation of a class of functions useful in the phase-integral approximation. i. results," *Journal of Computational Physics*, vol. **10**, no. 2, pp. 308–315, 1972.

[12] J. Gustavus, "Calculation of even order N's used in the fröman phase-integral approximation." Math. 401 class paper, Texas A&M University, 1991.

[13] J. Čížek, E. J. Weniger, P. Bracken, and V. Špirko, "Effective characteristic polynomials and two-point padé approximants as summation techniques for the strongly divergent perturbation expansions of the ground state energies of anharmonic oscillators," *Physical Review E*, vol. **53**, no. 3, p. 2925, 1996.

[14] B. Fornberg, "Generation of finite difference formulas on arbitrarily spaced grids," *Mathematics of Computation*, vol. **51**, no. 184, pp. 699–706, 1988.

[15] C. Taylor, "Finite difference coefficients calculator." https://web.media.mit.edu/~crtaylor/calculator.html, 2019.

[16] G. H. Golub and C. F. Van Loan, *Matrix Computations*. Johns Hopkins studies in the mathematical sciences, Baltimore: The Johns Hopkins University Press, fourth ed., 2013.

[17] Texas A&M High Performance Research Computing, *Terra User's Guide*.